Journal of Materials Chemistry C

ROYAL SOCIETY OF CHEMISTRY

PAPER

View Article Online
View Journal | View Issue

Cite this: J. Mater. Chem. C, 2025, 13, 22278

Deciphering the crystal structure evolution from 3D non-van der Waals solids to 2D nanosheets

V. M. Swathi,[a] Anjana E Sudheer,[b] G. Tejaswini,[b] Muthu Vallinayagam,[cd] T. Pandiyarajan,[b] D. Murali,[b] Matthias Zschornak*[cd] and Aji A. Anappara*[a]

Received 6th July 2025,
Accepted 1st October 2025

DOI: 10.1039/d5tc02585k

rsc.li/materials-c

Two-dimensional (2D) materials research has predominantly focused on quantum-confinement effects like energy discretisation and momentum-space broadening, regardless of whether they are derived from layered, van der Waals (vdW) materials or 3D-bonded, non-vdW solids. Fragmentation of bulk non-vdW materials to realise 2D nanosheets perturbs the interatomic forces and the atomic coordination, inducing intrinsic strain in the resulting 2D nanosheets. The subsequent strain-relaxation can lead to distinct atomic arrangements within the nanosheets, altering their macroscopic properties compared to the bulk counterpart. This work investigates the largely unexplored impact of fragmentation-induced strain on the crystal structure of free-standing 2D nanosheets derived from non-vdW solids, using orthorhombic sulfur (cyclo-S_8) as a model system. Using first-principles density functional theory (DFT) calculations, we predict two 2D allotropes of sulfur (designated "sulfurene"); a metastable α-sulfurene (α-S) phase, with a three-atom-layer 1T-MoS_2-like structure and a stable tetragonal β-sulfurene (β-S) phase. The allotropes are further experimentally realised *via* shear-assisted fracturing of elemental, bulk sulfur (orthorhombic cyclo-S_8) in an aqueous medium. Our findings demonstrate that fragmentation-induced structural modifications dominate the macroscopic characteristics of low-dimensional systems derived from non-vdW solids, opening avenues for discovering unprecedented optoelectronic functionalities.

Introduction

In a crystal, structural stability hinges on a delicate balance of interatomic forces, governed by factors such as the nature of atomic bonding, coordination number (CN), bond strength, and lattice energy.[1–3] This balance dictates the potential energy minima configuration of the crystal, resulting in well-defined structures characterised by specific lattice parameters, bond angles, and nearest-neighbour configurations. These structural features, in turn, determine the electronic band structure and the macroscopic traits of the material. When a crystal in thermodynamic equilibrium is subjected to external stimuli, such as pressure, temperature, electric field, or magnetic field, the equilibrium lattice parameters and CN can be significantly altered, leading to substantial modifications in the electronic band structure and, consequently, the macroscopic properties of the material. Respective examples have been theoretically predicted and experimentally demonstrated across diverse material systems. For instance, the high-pressure transformation of hexagonal graphite to cubic diamond (10 GPa, at 3000 °C), where the initial interlayer spacing in graphite critically influences the grain size of the resulting diamond, illustrates the profound impact of pressure on crystal structure and properties.[4] Similarly, molecular iodine undergoes an increase in CN from one to six and a subtle reduction in the lattice parameters at pressure exceeding 16 GPa, accompanied by a pressure-induced transition to a metallic state, enabling metallic conductivity.[5] Other notable examples include pressure-induced phase transitions in transition metal dichalcogenides (TMDs) often resulting in band gap closure and enhanced conductivity;[6–9] and the metal–insulator transition in vanadium dioxide (VO_2) at 340 K, characterised by a change in CN from 2 to 6 and a structural transformation from monoclinic to tetragonal rutile.[10] Moreover, external electric fields can induce structural deformation in lead-free piezoelectric ceramics, potentially driving phase transitions, such as from orthorhombic to tetragonal phases, which can enhance piezoelectric properties.[11] At the same time, electric-field-induced biaxial strain, which elongates or contracts the lattice parameters of TMDC single layers, can be utilised

[a] Photonic Materials and Devices Laboratory, Department of Physics, National Institute of Technology, Calicut, Kozhikode 673601, Kerala, India. E-mail: aji@nitc.ac.in
[b] Department of Sciences, Indian Institute of Information Technology Design and Manufacturing Kurnool, 518007, Andhra Pradesh, India
[c] Technical Physics, University of Applied Sciences, Friedrich-List-Platz 1, D-01069 Dresden, Germany. E-mail: matthias.zschornak@physik.tu-freiberg.de
[d] Institute of Experimental Physics, TU Bergakademie, Freiberg, Leipziger Str. 23, D-09596 Freiberg, Germany

to systematically tune their optoelectronic and photocatalytic properties, enhancing their HER performance.[12] Applying magnetic fields in $La_{0.85}Ce_{0.15}Fe_{12}B_6$ induces magnetoelastic coupling, driving a rhombohedral-to-monoclinic transition, consequently altering magnetic order and significantly impacting magnetoresistance, magnetostriction, and thermal expansion.[13] Similarly, applying a magnetic field during MnSe synthesis significantly impacted its properties. Increased field strength led to lattice strain, inducing structural transformations, including the formation of multiple rock salt phases and a morphological change from nanorods to cubes. This resulted in an increased energy gap and the emergence of insulating behaviour.[14] These cases collectively demonstrate that external stimuli-induced structural transformations in a crystal, caused by variations in inter-atomic distances or CN, can profoundly influence the mechanical, thermal, electronic, and optical properties of a crystal, significantly deviating from its behaviour in the initial thermal equilibrium state.

When 3D crystals are reduced to lower dimensions, such as 2D, naturally occurring layered materials are easily broken apart because, in these materials, strong in-plane covalent bonds hold atoms within each layer, while weak van der Waals (vdW) forces bind the layers together. This inherent layered structure facilitates the isolation of individual or few-layer nanosheets through various exfoliation techniques, such as mechanical cleavage or liquid exfoliation.[15–19] However, the properties of 2D materials derived from vdW solids are often primarily governed by quantum confinement effects and surface functionalisation, as the in-plane atomic arrangement is largely preserved during exfoliation. Unlike layered materials, non-layered crystalline materials have chemical bonds in all three dimensions, making it challenging to produce single layers due to the difficulty of breaking these strong bonds.[20] However, isolating a monolayer or a few layers from non-layered precursors like Au, CdS, LaB_6, elemental chalcogens and metal chalcogenides, has been demonstrated successfully and exhibits properties due to varying thickness and surface functionalisation, as we observed in layered 2D materials.[21–25] Beyond this, in non-van der Waals 3D-bonded solids, the dimensionality reduction from three to two-drastically alters the interatomic force balance. By the removal of interlayer interactions present in the bulk material, the remaining atoms within the 2D nanosheet experience a significant reduction in their coordination environment. Consequently, even in the absence of external stimuli, by forming the surfaces the mere process of isolating a monolayer or a few layers can induce intrinsic strain within the 2D sheet, leading to a relaxation towards a new equilibrium configuration where the in-plane forces are rebalanced, resulting in potential modifications to bond lengths, bond angles, and overall lattice parameters. Thermodynamically stable 2D nanostructures can be realised through this process provided that the atoms within the nanosheet can adapt to the modified coordination environment and lattice parameters. Given that the electronic band structure and macroscopic properties of a material are strongly correlated with its crystal structure, these structural modifications can, as pointed out above, lead to substantially altered properties compared to the corresponding bulk material.[21] This concept is exemplified by the various polymorphs of borophene, such as α-borophene, β_{12}-borophene, and χ^3-borophene, which exhibit distinct structural motifs and coordination environments, with boron atoms forming bonds with CN of 3, 4, 5, or 6.[26,27] This structural diversity significantly influences electronic properties, leading to phenomena such as Dirac fermions and superconductivity.[28,29] Previous studies on 2D materials, particularly those derived from layered vdW crystals, have primarily focused on size-quantisation effects and surface functionalisation, as exfoliation largely preserves the in-plane atomic arrangement. However, since less than 2.5% of known crystals exhibit weak vdW interactions, enabling easy downscaling *via* exfoliation, the majority of materials remain unexplored in their 2D forms.[30] This gap underscores the vast potential of investigating non-vdW crystals, where fragmentation-induced strain can significantly alter crystal parameters, a phenomenon that has received limited attention.

In this work, we demonstrate this phenomenon by investigating the fracturing of cyclo-S_8, a 3D-bonded molecular solid, into free-standing 2D nanosheets, and predict the existence of S-based 2D structures using DFT simulations. The metastable 1T-MoS_2-like α-S phase consists solely of planar four-membered rings of S atoms. In contrast, the stable tetragonal β-S phase exhibits a more intricate structure with both planar four-membered and chair-like six-membered rings arranged alternately. Electronic band structure calculations indicate that both α- and β-S are semiconductors with indirect band gaps of 1.4 eV and 3.62 eV, respectively. The optical properties were further investigated through computational analysis of the energy-dependent dielectric function to validate our arguments. In order to demonstrate the formation of free-standing 2D nanosheets from the bulk, we used cyclo-S_8, bulk sulfur powder in an orthorhombic crystal structure.[31,32] The nanosheets were realised by the shear-assisted fracturing technique *via* magnetic stirring with Polyethylene glycol (PEG-300) as a surfactant. The formation of the 2D phases is confirmed through high-resolution transmission electron microscopy (HRTEM) imaging of the nanosheets. The UV-vis absorption spectrum of the nanosheets reveals a sharp peak at 227 nm and a shoulder peak at 275 nm, likely due to edge or surface functionalisation. Fourier-transform infrared (FTIR) analysis confirmed that the 2D sulfur nanosheets (SNS) are inherently surface-functionalised with –OH groups and additional functional groups originating from PEG-300. Excitation wavelength-independent emission at 400 nm was observed for the SNS, likely arising from excess –OH functionalisation, with a red shift in the emission wavelength attributed to the PEG-300 functionalisation.

Experimental

Material

Sulfur pellets (99.998%) with a few mm in size were purchased from Sigma Aldrich and used as supplied without further purification. De-ionised (DI) water was used as a solvent, and

it was provided by the Merck Millipore DI water system. Polyethylene glycol (PEG-300) was used as the passivation agent. Dialysis tubing of a molecular weight cut of 12 kDa, and 1 kDa was supplied by Spectrum Laboratories, USA.

Instrumentation

The morphology and chemical composition were analysed using high-resolution scanning electron microscopy (HR-SEM). Transmission electron microscopy (TEM) images and selected area electron diffraction (SAED) images of the dispersion of sulfur nanostructures were recorded using a transmission electron microscope (Jeol 6390LA/OXFORD XMX N) to identify the morphology and crystal structure of the sample. High-resolution transmission electron microscopy measurements were also taken to analyse the atomic arrangement. The thickness of the samples is probed utilising AFM (Alpha300RA AFM). The crystallinity of the bulk sulfur and the sulfur nanostructures was studied using an X-ray diffractometer (Bruker D8 Advance: Cu Kα, λ = 1.54060 Å). The vibrational modes of the sulfur nanostructures and bulk sulfur were obtained by Raman microscope (Labram HR Evolution CCD Model:1024X256-OE) with a laser source of 532 nm. A Fourier transform infrared spectrometer detected the surface functional groups on sulfur nanostructures in ATR mode (SPECTRUM 2, PerkinElmer). UV-visible absorption Spectrometer (Shimadzu, Model: UV-2600) was used to measure the optical absorption. Photoluminescence (PL) spectra of sulfur nanostructures were collected *via* an LS-55 fluorescence spectrophotometer (PerkinElmer). The samples for TEM measurements were prepared by drop-casting aqueous sample onto a copper grid, and the solvent was dried under specific conditions. The FTIR measurements were carried out using powder bulk sulfur and aqueous dispersion of sulfur nanostructures in ATR mode. UV-vis spectra were obtained by using DI water as the solvent. AFM, XRD, and Raman studies were performed by drop-casting the aqueous dispersion of sulfur nanostructures onto a glass plate and drying at 50 °C. The dialysis process of sulfur nanosheets was carried out with the aid of a dialysis membrane of 12 kDa.

Method

Typically, 300 mg of bulk sulfur was ground in a mortar for 15 min without adding any solvent. The resulting dry sulfur powder was immediately dispersed in 50 mL of deionised (DI) water, followed by the addition of 3 mL of PEG-300. The mixture was stirred at a constant speed of 500 rpm for 72 h. After stirring, the sample was centrifuged at 2000 rpm for 15 min to separate the sulfur nanostructures from the residue. The clear and colourless supernatant was collected for further processing. The collected aqueous dispersion was dialysed against DI water for approximately three days using dialysis tubing with a molecular weight cut-off of 12 kDa under continuous magnetic stirring. The resulting clear dispersion inside the dialysis tubing was retained for subsequent studies. Morphological and microscopic characterisations revealed that the clear dispersion primarily consisted of 2D sulfur nanosheets, referred to as SNS. PEG-300 prevents restacking through surface adsorption, while control samples without PEG-300 showed rapid sedimentation and agglomeration (see the TEM images in Fig. S1).

Results and discussion

2D allotropes of sulfur

First-principles DFT calculations were employed to optimise the crystal structure of pristine S in both trigonal and orthorhombic phases. The orthorhombic phase was identified as the most stable configuration, with an energy of −4.23 eV per atom. Detailed lattice parameters (Table S1) and crystal structures (Fig. S2) are provided in Section SI of the SI. Section II presents a detailed morphological and crystalline analysis of bulk S, with additional information provided in Fig. S3 and S4 confirm the orthorhombic structure of S (see Table S2). Furthermore, using first-principles DFT calculations performed with the Vienna *Ab initio* Simulation Package (VASP)[33,34] (see Section SIII of SI for computational details), we predict a new class of 2D monolayers, designated as α-S, β-S, and γ-S (Fig. S5). In Fig. 1(a), planar four-membered rings of S are arranged in a 2D lattice of the α-S structure which resembles a 1T-MoS_2-like framework, where three S layers are present: the central layer (Mo position) exhibits metallic behaviour, while the outer layers (S positions, at the top and bottom) demonstrate semiconductor-like properties. A distinctive feature of α-S is its unique multivalency, with the outer S atoms exhibiting three-fold and the central six-fold coordination markedly different from the two-fold coordination commonly observed in bulk S. Fig. 1(a) and (b) illustrate the top and side views of α-S, providing insights into its atomic configuration. The 2D β-S structure was designed and geometrically optimised, with its top view shown in Fig. 1(c). The lattice parameters were determined to be 4.4 Å and 4.6 Å. In this configuration, the central S atom is four-fold coordinated, while the upper and lower S atoms are three-fold coordinated. Various 2D phases of S were identified through a mild shear-induced fracturing technique. The synthesis of SNS using this approach is illustrated in Fig. S6. HRTEM was employed to analyse the atomic arrangement within the SNS further. The S atoms in the HRTEM images were annotated using a ball-and-stick model. Notably, the atomic arrangement observed in Fig. 1(d) closely corresponds to the top view of α-S, with a unit cell parameter of 3.3 Å × 3.3 Å. Additionally, the side view shown in Fig. 1(e) reveals a buckling height of 2.7 Å between adjacent sulfurene layers, further confirming the structural features of α-S. Fig. 1(f) confirms the unit cell parameters of tetragonal β-S, 4.4 × 4.6 Å, with details on lattice parameters and total energy provided in Table S3. For a detailed understanding of the SNS morphology, refer to Fig. S7, which includes additional TEM images, HRTEM, and the selected area electron diffraction (SAED) pattern, and its analysis is given in Section SVI of the SI.

The energetic stability of the 2D S phases was evaluated by calculating the energy per atom, as presented in Table S4. Among these, the 2D β-S phase was identified as the most stable, with an energy of −12.37 eV, surpassing both α-S and γ-S.

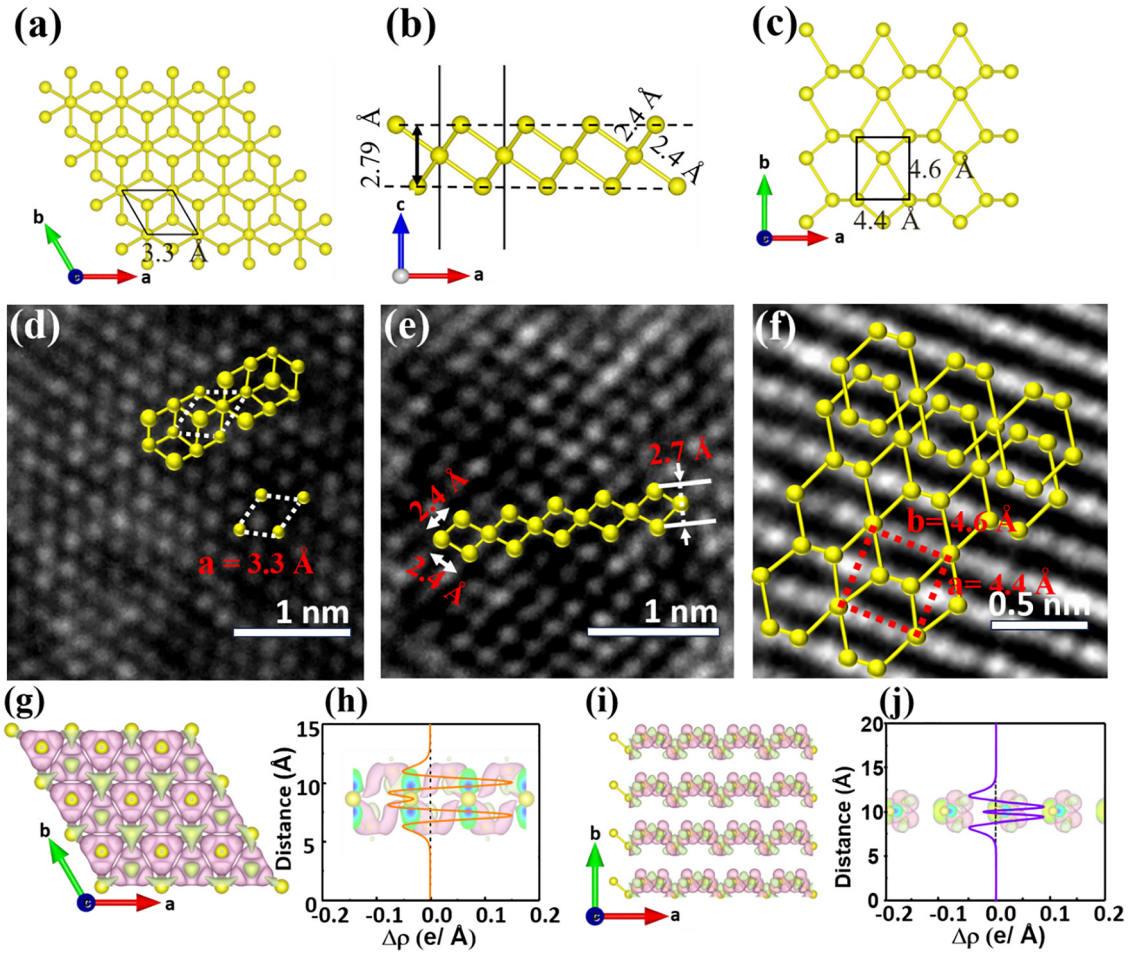

Fig. 1 (a) Top and (b) side views of optimised α-S monolayer, and (c) the top view of the optimised β-S monolayer. HRTEM images illustrate (d) the top and (e) side views of as-prepared SNS, confirming the 1T-MoS_2-like α-S structure; (f) depicts the top view of tetragonal β-S. Differential charge density plots for (g) α-S and (i) β-S monolayers with isosurface value 0.001 e $Å^{-1}$ are shown, where pink and green colours indicate charge accumulation and depletion, respectively. Planar-averaged electron density differences for the (h) α-S and (j) β-S monolayers.

The dynamical stability of the sulfurene monolayer was further assessed through analysis of phonon vibrational spectra. The absence of imaginary modes in the phonon spectra confirms the dynamical stability of the β-S monolayer (see Fig. S8b). In contrast, the α-S monolayer exhibits imaginary modes in its phonon spectra, which can be considered as a metastable state. The stability of these 2D phases may vary with temperature or under external conditions such as finite stress, strain, or pressure, potentially influencing their stabilisation in specific environments. To investigate charge transfer between S-sublayers, we performed differential charge density analysis and planar-averaged electron density difference calculations for α-S and β-S monolayers, as shown in Fig. 1(g)–(j). In α-S, charge is depleted from the middle layer and accumulates in the top and bottom layers. Bader charge analysis, presented in Table S5, quantifies this charge transfer, revealing a small charge redistribution of $+0.35e$ and $-0.17e$, indicative of the covalent bonding nature. In contrast, charge transfer between the S-sublayers in β-S is minimal compared to α-S, highlighting the strong covalent nature of S–S bonds within the β-S layer. The lower charge transfer suggests more charge dispersion in the interstitial regions, which may enhance the charge transport properties of β-S. Moreover, differential charge density analysis depicted in Fig. S9a–d revealed interlayer charge accumulation, confirming the presence of interlayer interactions that vary between α-S and β-S.

The building blocks of elemental S, cyclo-S_8 rings, are inherently non-layered. The interactions between these fused rings in the orthorhombic structure are found to be weak. Sulfur's preference for a puckered, closed-ring structure over a planar, graphene-like arrangement can be attributed to its two extra valence electrons compared to carbon. These additional electrons alter bonding characteristics, stabilising the crown-like configuration instead of a flat structure. Breaking the non-layered, closed-ring structure and reconfiguring it into parallel layered arrangements to achieve a 2D sulfurene structure poses significant challenges. To explore the feasibility of forming 2D and 1D S nanostructures experimentally, their energetic stability was investigated. The energy per atom for various dimensional S nanostructures was calculated and is

presented in Table S5 and Fig. S10. The results show comparable energies among the phases, indicating that with controlled energy input, the S_8 fused rings can be opened to form 2D layered structures. Among these, the 2D β-S layered structure exhibits an energy closest to that of the orthorhombic structure of S, making the transition between these phases energetically favourable.

Additionally, the 1D S nanostructure, described as helical chains (see Fig. S9a and b), can be derived from the 2D β structure. By supplying additional energy to the system, the transition from the 2D β-S layered structure to the 1D helical structure is achievable, suggesting the possibility of a 2D-to-1D structural transformation. Phonon spectra analyses of both the 1D helical chain (Fig. S11c) and (2D β-S Fig. S8b) reveal the absence of imaginary modes, confirming their dynamical stability. Moreover, a phase transition from the α to β structure under strain or pressure has been reported for Te.[35,36] A similar transformation is expected in 2D S layers, which may account for the experimentally synthesised structures being a mixture of α and β phases. In consequence, the further computational analysis of electronic properties focuses on the α and β phases and omits the γ-phase.

Physico-chemical properties of SNS

Atomic force microscopy (AFM) was employed to investigate the topographical morphology of SNS, as illustrated in Fig. 2(a). The optimised structure of bilayer α-S, depicted in Fig. 2(b), reveals an interlayer distance of 3.26 Å. Additionally, the buckling height of a single α-S layer, measured at 2.79 Å, suggests that the overall thickness of the bilayer could approximate 8.84 Å. Height profile analysis, presented in Fig. 2(a), indicates nanosheet thicknesses of approximately 0.87 nm, 0.9 nm, and 1.05 nm. These findings confirm that the SNS analysed in panels (a) and (b) are consistent with the theoretical thickness of bilayer α-S. Compared to the bulk counterpart, the XRD patterns of SNS in Fig. 2(c) show prominent peaks at (111), (220), (222), (026), (313), and (044), which are in good agreement with the orthorhombic S. Furthermore, the XRD patterns of SNS exhibit noticeable peak broadening at 2θ = 11.38°, 21.78°, 22.97°, 26.61°, 28.55°, 34.79° compared to bulk orthorhombic S, as shown in Fig. S12. This broadening is indicative of reduced crystallite size, and increased lattice strain suggests fragmentation-induced structural perturbations during the size reduction of bulk S.

As shown in Fig. 2(d), the Raman spectrum of bulk S exhibits three prominent peaks at 153.8 cm^{-1}, 219.3 cm^{-1}, and 473.3 cm^{-1}, corresponding to its orthorhombic structure.[37] The peaks at 153.8 cm^{-1} and 219.3 cm^{-1} are attributed to the anti-symmetric and symmetric bond-bending modes of S, respectively, while the peak at 473.3 cm^{-1} corresponds to

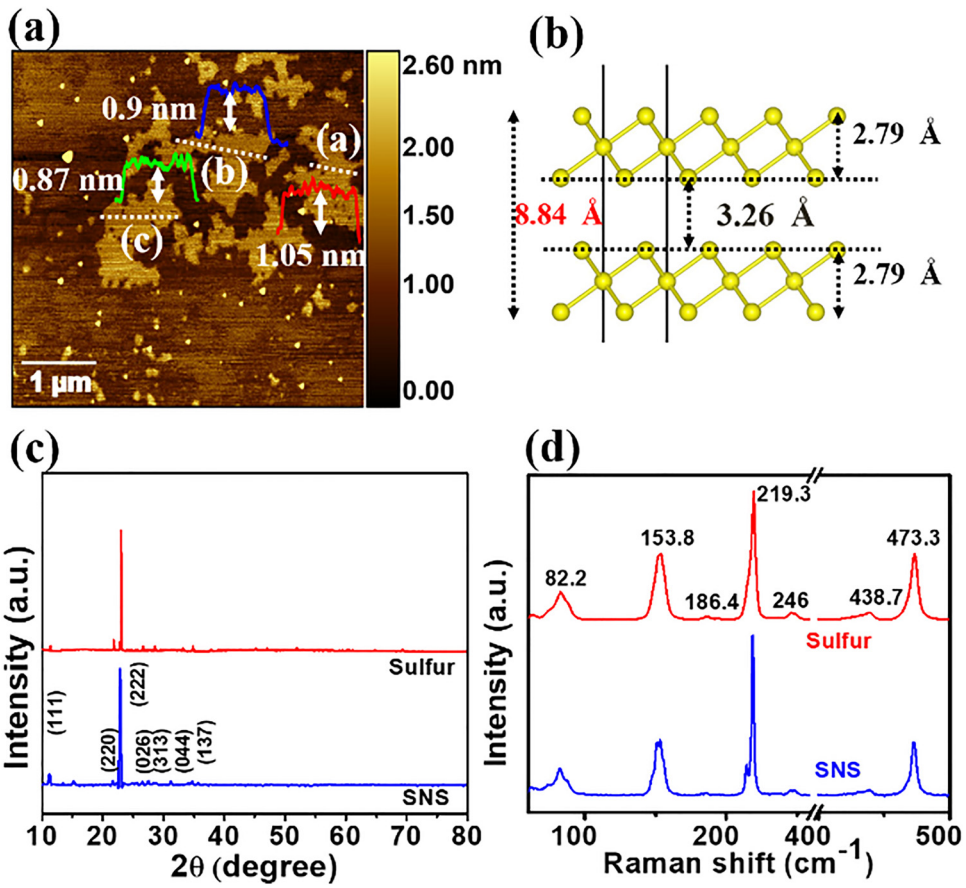

Fig. 2 (a) AFM image of SNS with the insets showing the height profiles along with (b) the side view of bilayer α-S, indicating the spacing between the layers. (c) XRD patterns and (d) Raman spectra of the SNS give a comparison to bulk S.

the symmetric S–S bond-stretching mode of the S_8 rings.[38,39] The Raman spectrum of SNS closely resembles that of bulk orthorhombic S, but shows broadened and split peaks compared to the peaks of bulk S. Especially, splitting of the ~219.3 cm^{-1} mode suggests distortion in S_8 rings or formation of non-ring structures like S chains.[40–42] The deconvolution of the peak located at 219.3 cm^{-1} for both bulk sulfur and SNS is presented in Fig. S13. In the case of bulk sulfur, the deconvoluted spectrum reveals a shoulder at 217.8 cm^{-1} alongside the main peak at 219.3 cm^{-1}. For SNS, a shift toward lower wavenumbers is observed, with the deconvoluted peaks appearing at 218.7 cm^{-1} and 216.7 cm^{-1}. Additionally, a new peak emerges at 214.2 cm^{-1} indicating further peak splitting and suggesting structural modifications in the nanosheet form.

Fig. S14 indicates the FTIR data obtained for SNS and PEG-300 in the range of 500–4000 cm^{-1}. The band at around 2865 cm^{-1}, attributed to the C–H stretching vibrations of the $-CH_2$ group, shifts to 2925 cm^{-1} in SNS as shown in Fig. S14.[43] This shift is likely due to the difference between pure PEG-300 and the surface-modified SNS with PEG-300. Moreover, the absorption bands at SNS show similar characteristic features of PEG. This suggests that PEG-300 has modified the surface of SNS without any chemical reactions.

Optical properties

To investigate the electronic properties of the sulfurene monolayer, the electronic band structures were calculated. In Fig. S15a, the GGA-level calculation reveals an indirect bandgap of 0.76 eV for α-S, with the conduction band minimum (CBM) located at the Γ point and the valence band maximum (VBM) between the Γ and K points. Since GGA tends to underestimate band gaps, further calculations were performed using the hybrid HSE functional. The HSE band structure, presented in Fig. 3(a) indicates a larger bandgap of 1.4 eV. The electronic properties of the 2D β-S structure were also investigated (see Fig. S15c and Fig. 3(b)). The results indicate an indirect bandgap with values of 2.46 eV and 3.62 eV. In the band structure, the CBM is located between the high-symmetry *k*-points X and S. At the same time, the VBM lies between the S and Y points. Compared to the electronic band structure of the α-S structure, the β-S structure exhibits less band dispersion, indicating lower charge carrier mobility. The anisotropic dispersion of the valence and conduction bands suggests anisotropic transport properties for both electrons and holes. Such characteristics will likely reduce charge recombination, which could benefit applications requiring efficient charge separation. The electronic band structure of orthorhombic sulfur (see Fig. S15e) exhibits a dense distribution of bands, which is entirely different from that of α-S and β-S monolayers, with a band gap of approximately 2.2 eV.

The optical properties were explored by examining the energy-dependent dielectric function. The dielectric spectra for α-S and β-S monolayers are calculated using both GGA and HSE functionals and are depicted in Fig. 3(d) and (e). We extended our theoretical investigation to bilayer and trilayer α-S and β-S allotropes. The optical absorption spectra of multilayer structures, as shown in Fig. S16a and b, only show marginal changes compared to the monolayer, with a slight increase in intensity but no significant shift in the absorption

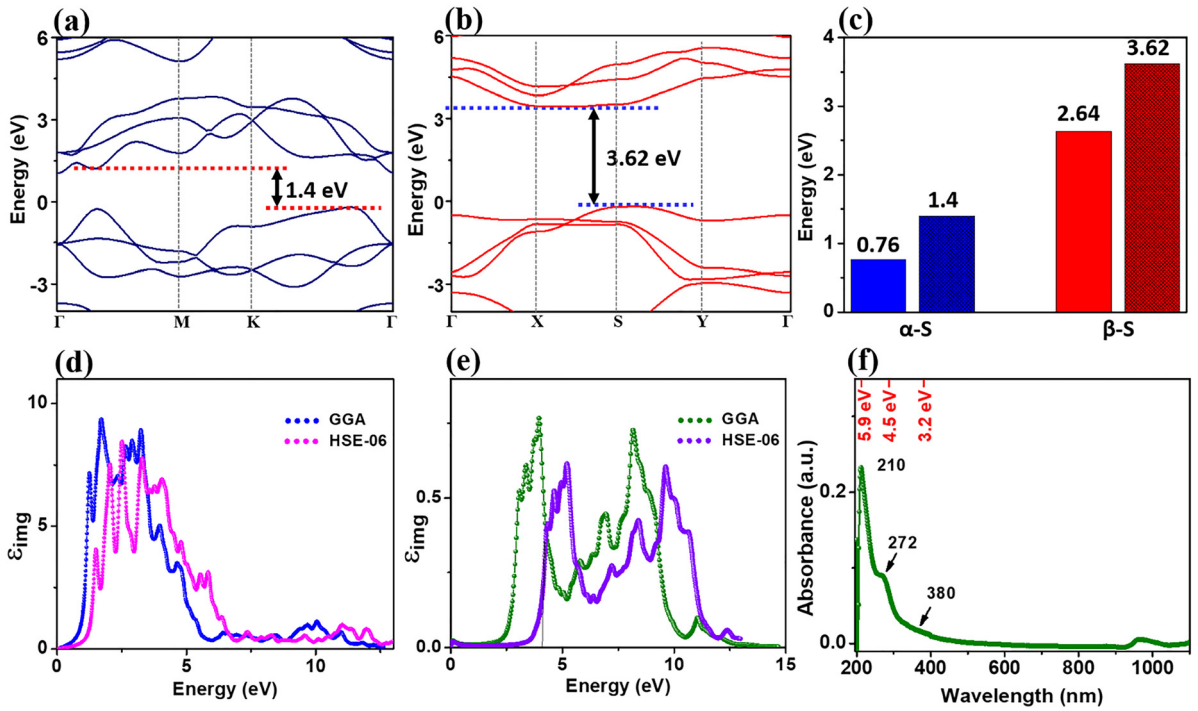

Fig. 3 Electronic band structure of monolayer (a) α-S and (b) β-S calculated using the HSE-06 functional. (c) Comparative analysis of the bandgaps of α-S and β-S, obtained using the GGA and HSE-06 functionals. Dielectric spectra of monolayer (d) α-S and (e) β-S have been calculated using the GGA and HSE-06 functionals. (f) UV-vis absorption spectrum of SNS using DI water as a reference.

region. The GGA results display intense peaks in the visible light range for α-S, whereas the HSE results show a shift to higher energy, with optical absorption occurring in the UV region. This shift reflects the influence of the wider bandgap in the HSE electronic band structure. The optical absorbance of the β-S monolayer was analysed based on the imaginary part of the dielectric function, as computed using both GGA and HSE-level methods. The absorption spectra derived from GGA calculations exhibit a broad optical absorption spanning the visible to UV regions. In contrast, the spectra obtained using the HSE approximation reveal a blue shift in absorption, with the primary features shifting toward higher energy, predominantly in the UV range. Thus, the distinct crystal structures of α-S and β-S enable the exploration of their diverse optoelectronic properties. In parallel, the optical properties of SNS have been analysed within the UV-visible absorption region, with DI water as the reference solvent. The absorption peaks for SNS are observed at 210 nm, 272 nm, and 400 nm, as shown in Fig. 3(f), whereas bulk S exhibits optical absorption predominantly in the deep UV region, extending up to 500 nm in the visible range (see Fig. S17a in SI). Explaining the possible origins of these absorption bands of SNS, heteroatoms S, and O (oxygen) contain non-bonding electrons, and the n → σ* transition usually has an absorption in the range of 150–250 nm.[44] The band at 380 nm may be attributed to the presence of coordinated sulfur species, while the shoulder centred at 272 nm could be associated with different allotropic forms of S, as reported in previous literature.[44–47] Fig. S18a demonstrates the stability of the dispersion of SNS over one month. Moreover, zeta potential measurements conducted on freshly prepared SNS and samples aged for one month confirm the stability of the nanosheet dispersion in the DI water-PEG-300 mixture (see Fig. S13b and c in SI).

Photoluminescence (PL) of the SNS shows considerable emission at the violet region (400 nm), illustrated in Fig. 4(a). Examining the PL characteristics of SNS, it is noted that the spectra exhibit smooth and narrow peaks, with a full-width half maximum of 70 nm. The excitation spectrum in Fig. 4(b) reveals two significant peaks at 217 nm and 290 nm, which closely match the absorption spectrum of the SNS. In Fig. 4(a), the emission peak at 400 nm remains constant when the excitation wavelength (λ_{ex}) ranges from 220 nm to 300 nm (see Fig. S19 in SI). However, as λ_{ex} exceeds 300 nm, a redshift in the emission wavelength (λ_{em}) is observed, reaching up to 430 nm. SNS can be surface/edge functionalised with hydroxyl (–OH) groups derived from DI water, as well as functional groups from PEG-300. The excitation-wavelength-independent emission at 400 nm up to λ_{ex} of 300 nm, indicating a single chromophore domain, possibly arising from –OH functionalisation.[48] A slight redshift in the emission peak indicates functionalisation from PEG-300, which can act as different emission centres depending on the change in excitation wavelength.[49] Additionally, an emission peak at 590 nm was detected, primarily at excitation wavelengths of 210 and 260 nm, as shown in Fig. 4(c). The corresponding

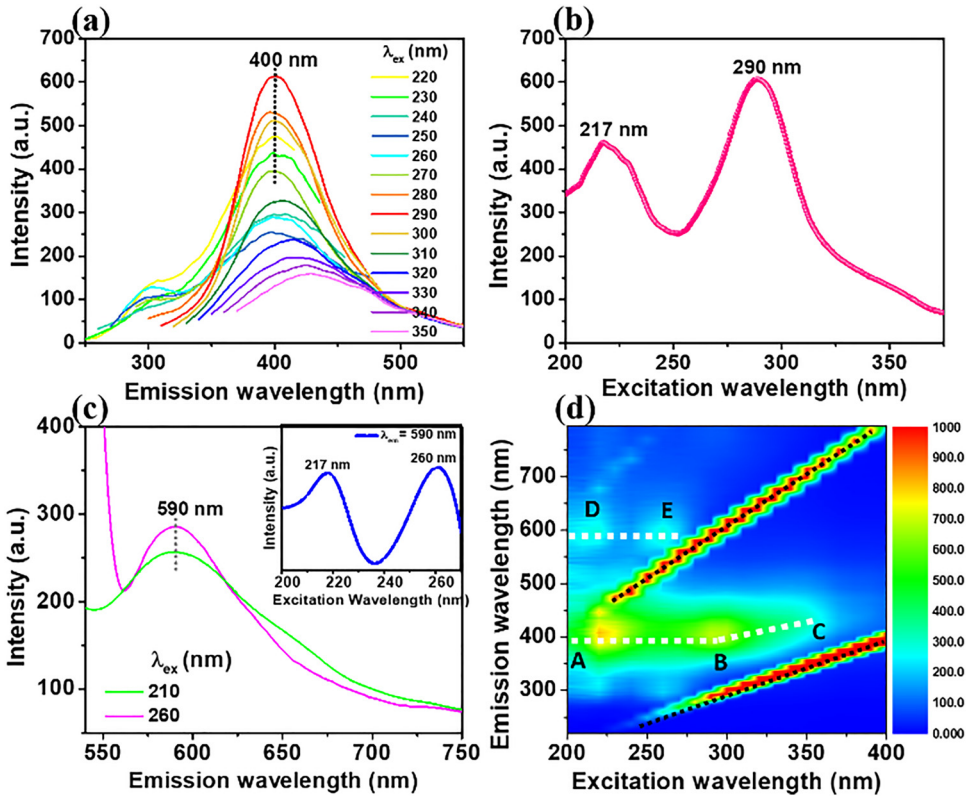

Fig. 4 (a) PL spectra of SNS at excitation wavelengths in the range of 220–350 nm (b) excitation spectrum at λ_{em} = 400 nm, and (c) emission spectra at λ_{em} = 590 nm (inset: excitation spectrum at λ_{em} = 590 nm), (d) Contour plot of SNS obtained from the excitation–emission wavelength matrix.

excitation spectrum is provided in the inset. This emission behaviour is observable from the horizontal white dotted line DE in the contour plot obtained from the excitation–emission matrix in Fig. 4(d). The contour plot indicates that the emission is primarily concentrated around 400 nm from A to B (represented by a second white dotted line in Fig. 4(d)). A slight red shift in the emission peaks was observed beyond the excitation wavelength of 300 nm, as represented by the line BC. To further confirm the presence of multiple emission centres, lifetime measurements (see Section SXVIII of SI) of SNS were performed at excitation λ_{ex} of 295 nm and 330 nm. The results revealed a triple-exponential decay at emission wavelengths of 400 nm and 420 nm, indicating the involvement of multiple emissive sites in the PL process. The PL lifetime was analysed using a triple-exponential fitting function, with the fitting parameters detailed in Table S6. The average lifetime of SNS was approximately 8.6 ns at an excitation wavelength of 295 nm, which decreased to 4.1 ns when the excitation wavelength was increased to 330 nm, as shown in Fig. S20a and b. In addition, the quantum yield (QY), a measure of the efficiency of photon emission, was calculated using quinine sulphate as a reference. The resulting QY was 12.6%, with detailed calculations provided in Section SXIX of SI. This work challenges the conventional focus on quantum confinement and surface effects in 2D materials by investigating fragmentation-induced strain in non-van der Waals 3D-bonded solids. Using a combined DFT and experimental approach, we predict and confirm the formation of novel 2D S allotropes (α-S and β-S) from cyclo-S_8, demonstrating that this strain leads to distinct structural modifications and optoelectronic properties, expanding the scope of 2D material synthesis.

Conclusions

In conclusion, this work demonstrates a novel pathway for generating 2D materials with tailored properties by fracturing non-van der Waals 3D-bonded solids. We have shown that disintegration of the bulk induces strain, leading to the formation of distinct allotropes of 2D S: a metastable 1T-MoS_2-like α-S phase and a stable tetragonal β-S phase, each with unique structural and optoelectronic characteristics. Computational analysis of the electronic band structure reveals that both allotropes exhibit semiconducting behaviour, with indirect band gaps of 1.4 eV and 3.62 eV for α-S and β-S, respectively. Analysis of the energy-dependent dielectric function further supports these findings, indicating potential for optoelectronic applications. Crucially, these theoretical predictions were experimentally validated by fabricating 2D SNS using a shear-assisted fracturing technique with PEG-300 as a surfactant. HRTEM confirmed the presence of both α-S and β-S phases within the synthesised SNS, providing direct experimental evidence for the successful isolation of novel 2D allotropes from a non-layered precursor. The successful synthesis of novel 2D S-based allotropes demonstrates the potential of this approach to unlock unprecedented functionalities and broaden the applications of 2D materials beyond the traditional van der Waals paradigm.

Conflicts of interest

The authors have no conflicts to disclose.

Data availability

The data that support the findings of this study are available within the article and its supplementary information (SI). Supplementary information: Details of the crystal structure, FESEM, XRD, and the UV-Visible absorption spectrum (in DRS mode) of pristine S, including computational details. Additional TEM images, SAED patterns with their indexing, computational methodology, phonon band dispersion, FTIR, electronic band-structures, zeta potential, photoluminescence quantum yield calculations, and lifetime calculations of 2D sulfurene. See DOI: **https://doi.org/10.1039/d5tc02585k**.

Acknowledgements

The fellowship of Ms Swathi V. M. by the University Grants Commission (UGC), New Delhi, India, is gratefully acknowledged. We extend our gratitude to Dr Lakshmi C. from the Organic Chemistry Lab, Department of Chemistry, NIT Calicut, for assisting with PL measurements. We also thank Ms Selvi from the Amrita Centre for Nanoscience and Molecular Medicine, Kochi, for obtaining the HRTEM images, the Analytical Instrumentation Facility (SAIF) at MG University, Kottayam, for TCSPC measurements, the Central Sophisticated Instrumentation Facility (CSIF) at the University of Calicut for providing experimental facilities for AFM analysis, Department of Physics, NIT Calicut, for XRD measurements (FIST, grant no. SR/FST/PSI-113/2019), School of Material Science and Engineering, NIT Calicut for Raman analysis. G. Tejaswini, and D. Murali acknowledge funding by the DST-SERB within the projects CRG/2022/006778. Matthias Zschornak and Muthu Vallinayagam thank to Technical Physics, University of Applied Sciences, Friedrich-List-Platz 1, D-01069 Dresden, Germany and the Institute of Experimental Physics, TU Bergakademie Freiberg, Leipziger Str. 23, D-09596 Freiberg, Germany, for the computational facility.

References

1 A. F. Wells, *Nature*, 1971, **229**, 453.
2 L. Pauling, *An Introduction to Modern Structural Chemistry*, Cornell University Press, 1960.
3 A. F. Kapustinskii, *Q. Rev., Chem. Soc.*, 1956, **10**, 283–294.
4 H. Xie, F. Yin, T. Yu, J.-T. Wang and C. Liang, *Sci. Rep.*, 2014, **4**, 5930.
5 M. Pasternak, J. N. Farrell and R. D. Taylor, *Phys. Rev. Lett.*, 1987, **58**, 575–578.

6 Z. Zhao, H. Zhang, H. Yuan, S. Wang, Y. Lin, Q. Zeng, G. Xu, Z. Liu, G. K. Solanki, K. D. Patel, Y. Cui, H. Y. Hwang and W. L. Mao, *Nat. Commun.*, 2015, **6**, 1–8.
7 Y. Gao, C. Liu, C. Tian and C. Zhu, *Chin. Phys. B*, 2024, **33**, 1–5.
8 A. Castellanos-Gomez, R. Roldán, E. Cappelluti, M. Buscema, F. Guinea, H. S. J. van der Zant and G. A. Steele, *Nano Lett.*, 2013, **13**, 5361–5366.
9 P. Johari and V. B. Shenoy, *ACS Nano*, 2012, **6**, 5449–5456.
10 A. Zylbersztejn and N. F. Mott, *Phys. Rev. B*, 1975, **11**, 4383–4395.
11 W. Feng, H. Du, C. Chen and Y. Huang, *J. Am. Ceram. Soc.*, 2016, **99**, 135–140.
12 Z. Liu, B. Wang and C. Cazorla, *ACS Sustainable Chem. Eng.*, 2022, **10**, 16924–16934.
13 L. V. B. Diop, T. Faske, O. Isnard and W. Donner, *Phys. Rev. Mater.*, 2021, **5**, 104401.
14 A. S. Nokabadi and A. Yazdani, *Nanoscale Adv.*, 2023, **5**, 6170–6176.
15 Y. Lin, T. V. Williams and J. W. Connell, *J. Phys. Chem. Lett.*, 2010, **1**, 277–283.
16 X. Huang, Z. Zeng and H. Zhang, *Chem. Soc. Rev.*, 2013, **42**, 1934–1946.
17 M. Chhowalla, H. S. Shin, G. Eda, L. J. Li, K. P. Loh, H. Zhang, Y. Lin, T. V. Williams and J. W. Connell, *Nat. Chem.*, 2010, **1**, 277–283.
18 B. Feng, J. Zhang, Q. Zhong, W. Li, S. Li, H. Li, P. Cheng, S. Meng, L. Chen and K. Wu, *Nat. Chem.*, 2016, **8**, 563–568.
19 H. Liu, Y. Du, Y. Deng and P. D. Ye, *Chem. Soc. Rev.*, 2015, **44**, 2732–2743.
20 Y. Sun, Z. Sun, S. Gao, H. Cheng, Q. Liu, J. Piao, T. Yao, C. Wu, S. Hu, S. Wei and Y. Xie, *Nat. Commun.*, 2012, **3**, 1057.
21 N. Zhou, R. Yang and T. Zhai, *Mater. Today Nano*, 2019, **8**, 100051.
22 S. K. John and A. A. Anappara, *RSC Adv.*, 2020, **10**, 31788–31793.
23 V. M. Swathi, K. Arjun, A. Rajan, R. Chatanathodi, K. Balasubramanian and A. A. Anappara, *Phys. Chem. Chem. Phys.*, 2024, **26**, 22112–22121.
24 A. Bhui, S. Roychowdhury, A. Sen, U. V. Waghmare and K. Biswas, *Z. Anorg. Allg. Chem.*, 2022, **648**, e202200097.
25 C. Tan and H. Zhang, *Nat. Commun.*, 2015, **6**, 7873.
26 X. Wu, J. Dai, Y. Zhao, Z. Zhuo, J. Yang and X. C. Zeng, *ACS Nano*, 2012, **6**, 7443–7453.
27 L. Bignardi, M. Pozzo, A. Zelenika, F. Presel, P. Lacovig, S. Lizzit, D. Alfè and A. Baraldi, *Surf. Interfaces*, 2024, **51**, 104791.
28 X.-F. Zhou, X. Dong, A. R. Oganov, Q. Zhu, Y. Tian and H.-T. Wang, *Phys. Rev. Lett.*, 2014, **112**, 85502.
29 Y. Zhao, S. Zeng and J. Ni, *Appl. Phys. Lett.*, 2016, **108**, 242601.
30 H. Gao, Z. Wang, J. Cao, Y. C. Lin and X. Ling, *ACS Nano*, 2024, **18**, 16343–16358.
31 K. Y. Andrew Lin and Z. Y. Zhang, *RSC Adv.*, 2016, **6**, 15027–15034.
32 G. Liu, P. Niu, L. Yin and H.-M. Cheng, *J. Am. Chem. Soc.*, 2012, **134**, 9070–9073.
33 G. Kresse and J. Furthmüller, *Comput. Mater. Sci.*, 1996, **6**, 15–50.
34 G. Kresse and J. Furthmüller, *Phys. Rev. B: Condens. Matter Mater. Phys.*, 1996, **54**, 11169–11186.
35 Y. Xiang, S. Gao, R.-G. Xu, W. Wu and Y. Leng, *Nano Energy*, 2019, **58**, 202–210.
36 J. Wang, H. Shen, Z. Yu, S. Wang, Y.-Y. Chen, B.-R. Wu and W.-S. Su, *ACS Omega*, 2020, **5**, 18213–18217.
37 P. Liu, J. M. Gardner and L. Kloo, *Chem. Commun.*, 2015, **51**, 14660–14662.
38 K. Venkateswarlu, *Proc. – Indian Acad. Sci., Sect. A*, 1940, **12**, 453–462.
39 J. Xu, D. Su, W. Zhang, W. Bao and G. Wang, *J. Mater. Chem. A*, 2016, **4**, 17381–17393.
40 A. G. Kalampounias, K. S. Andrikopoulos and S. N. Yannopoulos, *J. Chem. Phys.*, 2003, **118**, 8460–8467.
41 A. T. Ward, *J. Phys. Chem.*, 1968, **72**, 4133–4139.
42 L. Zhang, Y. Ren, X. Liu, F. Han, K. Evans-Lutterodt, H. Wang, Y. He, J. Wang, Y. Zhao and W. Yang, *Sci. Rep.*, 2018, **8**, 4558.
43 M. Sahu, V. R. M. Reddy, B. Kim, B. Patro, C. Park, W. K. Kim and P. Sharma, *Materials*, 2022, **15**, 1–16.
44 Z. Bai, L. Shen, J. Wei, Y. Li, A. Abbas, Y. Li, M. Qu, D. Zhang and C. Zhang, *ACS Appl. Nano Mater.*, 2020, **3**, 10749–10756.
45 A. Mondal, R. Salampuriya, A. Umesh and M. De, *J. Mater. Chem. B*, 2024, **12**, 973–983.
46 Q. Zou and Y.-C. Lu, *J. Phys. Chem. Lett.*, 2016, **7**, 1518–1525.
47 L. Shen, J. Wei, Z. Liu, Z. Bai, Y. Li, D. Zhang and C. Zhang, *Chem. Mater.*, 2020, **32**, 10476–10481.
48 A. Mondal, R. Salampuriya, A. Umesh and M. De, *J. Mater. Chem. B*, 2023, **12**, 973–983.
49 C. Sun, X. Jiang, B. Li, S. Li and X. Z. Kong, *ACS Sustainable Chem. Eng.*, 2021, **9**, 5166–5178.

